Available online at www.sciencedirect.com
SCIENCE DIRECT®
Journal of Solid State Chemistry 178 (2005) 1661–1669
JOURNAL OF SOLID STATE CHEMISTRY
www.elsevier.com/locate/jssc

High-pressure synthesis of solid solutions between trigonal $LiNiO_2$ and monoclinic $Li[Li_{1/3}Ni_{2/3}]O_2$

Elitza Shinova[a], Ekaterina Zhecheva[a,*], Radostina Stoyanova[a], Geoffrey D. Bromiley[b,c]

[a]*Institute of General and Inorganic Chemistry, Bulgarian Academy of Sciences, Bldg. 11, BG-1113 Sofia, Bulgaria*
[b]*Bayerisches Geoinstitut, Universität Bayreuth, D-95440 Bayreuth, Germany*
[c]*Department of Earth Sciences, University of Cambridge, Cambridge CB2 3EQ, UK*

Received 17 January 2005; received in revised form 8 March 2005

Abstract

High-pressure synthesis in an oxygen-rich atmosphere yields solid solutions between $LiNiO_2$ and Li_2NiO_3 over the whole concentration range. Structural characterization of the high-pressure oxides was performed using powder XRD, SEM analysis, IR spectroscopy, EPR spectroscopy at 9.23 and 115 GHz and magnetic susceptibility measurements. The crystal structure of $Li[Li_xNi_{1-x}]O_2$,$0 \leqslant x \leqslant \frac{1}{3}$, changes from trigonal *R*-3*m* to monoclinic *C*2/*m* at Li-to-Ni ratio of 2 (or $x = \frac{1}{3}$). The incorporation of Li into NiO_2-layers causes a decrease in the mean Li-O and $Ni_{1-x}Li_x$–O bond distance. Li and Ni ions in the mixed $Ni_{1-x}Li_xO_2$-layers display a tendency to order at a short length scale in such a way that mimics the $Li_{1/3}Ni_{2/3}$-arrangment of the end $Li[Li_{1/3}Ni_{2/3}]O_2$ composition. The charge distribution in these oxides proceeds via Ni^{3+} and Ni^{4+} ions.

Keywords: Lithium nickelates; High-pressure synthesis in oxygen atmosphere; Electron paramagnetic resonance

1. Introduction

Lithium–nickel oxides ($LiNiO_2$) with layered crystal structure belong to the main family of electrode materials used in lithium-ion batteries, where reversible oxidation/reduction of the Ni^{3+}/Ni^{4+} ions takes place in the course of electrochemical lithium deintercalation/intercalation [1–3]. The intercalation properties of $LiNiO_2$ have been shown to depend strongly on the structural characteristics of the LiO_2-layers. Based on X-ray diffraction (XRD) and neutron diffraction studies, it has been found that Ni ions in an oxidation state of 2+ fill the depleted LiO_2-layers in nearly stoichiometric $Li_{1-\delta}Ni_{1+\delta}O_2$. The appearance of extra Ni ions in the LiO_2-layers complicates the extraction of Li, as a result of which non-stoichiometric lithium nickelates display poor electrochemical performance as cathode materials in lithium ion batteries. The synthesis procedure of $LiNiO_2$ includes mixing of appropriate amounts of Li and Ni-salts, followed by heat treatment at 700 °C in an oxidative atmosphere [4–7]. At this temperature, there are two competitive reactions: solid state interaction between Li- and Ni-salts and Li evaporation. To compensate for the Li evaporation during the synthesis procedure, the initial Li-salt is taken in excess in respect to the stoichiometric one. Even at these experimental conditions, non-stoichiometric $Li_{1-\delta}Ni_{1+\delta}O_2$ oxides, where δ varies between 0.01 and 0.05, have been formed [4,7].

By increasing the oxygen pressure, it has been reported that extra Li ions can be incorporated in the NiO_2-layers. When Li-to-Ni ratio is 2, a layered lithium nickelate with the composition Li_2NiO_3 has been prepared under 150 bar in an oxygen-rich atmosphere by Migeon et al. [8]. The charge compensation is achieved by stabilization of highly oxidized Ni^{4+} ions. The structure of Li_2NiO_3 is composed of pure Li layers and mixed Li/Ni layers. The lithium and nickel ions are ordered in the mixed layers, leading to a reduction in the space group symmetry from *R*-3*m* to *C*2/*c* [8]. The main

*Corresponding author. Fax: +359 2 870 50 24.
E-mail address: zhecheva@svr.igic.bas.bg (E. Zhecheva).

0022-4596/$ - see front matter © 2005 Elsevier Inc. All rights reserved.
doi:10.1016/j.jssc.2005.03.007

structural difference between $LiNiO_2$ and Li_2NiO_3 is associated with the nickel-rich layers. For layered $LiNiO_2$, pure NiO_2-layers exist, whereas for monoclinic Li_2NiO_3 mixed $[Li_{1/3}Ni_{2/3}]O_2$-layers are developed, in addition to the pure LiO_2-ones. In addition, the layered oxide with Li_2NiO_2 composition has been prepared by electrochemical insertion of extra Li in the LiO_2-layers of $LiNiO_2$ [9]. The incorporation of Li leads to the collective transition of all Li^+ ions from octahedral to tetrahedral positions. Contrary to Li_2NiO_3, the charge compensation is achieved by Ni^{2+} ions.

For pressures between 2 and 4 GPa, formation of $Li[Li_xNi_{1-x}]O_2$ with $x \approx 0.12$ has been reported [10]. These compositions display different electrochemical properties compared to layered $LiNiO_2$. Moreover, the electrochemical behavior of $Li[Li_xNi_{1-x}]O_2$ is rather close to that of electrodes based on "$LiNiO_2$–Li_2MnO_3" oxides. Recently, complex "$LiNiO_2$–Li_2MnO_3" oxides have been considered as most perspective electrode materials for lithium-ion batteries [3,11–16]. The structure of "$LiNiO_2$–Li_2MnO_3" oxides is still unclear. Based on the careful XRD analysis, Dahn et al. have been suggested that $LiNiO_2$ and Li_2MnO_3 oxides form solid solution phases [14]. Analysis of the MAS-NMR spectra and lattice imaging by TEM have been interpreted in terms of the structure integration of monoclinic Li_2MnO_3 into layered $LiNiO_2$ leading to complex domain structure of "$LiNiO_2$–Li_2MnO_3" oxides [16].

The main goal of this paper is to study the formation of a solid solution between trigonal $LiNiO_2$ and monoclinic $Li[Li_{1/3}Ni_{2/3}]O_3$. For the preparation of new $yLiNiO_2.(1-y)Li[Li_{1/3}Ni_{2/3}]O_2$ compositions, we have considered a synthetic procedure involving a solid-state reaction between Li_2O_2 and NiO under high-pressure in an oxygen-rich atmosphere, intended to stabilize Li^+ ions in the nickel layers. XRD powder analysis, scanning electron microscopy (SEM) and IR spectroscopy were used for structural characterization of the mixed $[Li_xNi_{1-x}]O_2$-layers. The oxidation state of nickel ions was determined by chemical analysis, electron paramagnetic resonance (EPR) of Ni^{3+} and magnetic susceptibility measurements.

2. Experimental

Compositions of $Li[Li_xNi_{1-x}]O_2$ were prepared by a solid state reaction between NiO (obtained by thermal decomposition of $Ni(OH)_2$ at 550 °C) and Li_2O_2 (Aldrich) at 3 GPa and 700 °C for 2.5 h. High-pressure synthesis was performed using a $\frac{1}{2}$ in end-loaded piston-cylindrical apparatus at the Bayerisches Geoinstitut. Samples were encapsulated in 1 cm long, 5 mm diameter welded Pt capsules. The capsules were surrounded by a pyrophyllite sample holder and inserted into talc–pyrex cells with a tapered graphite-resistance heater. Pressure was calibrated against the quartz–coesite and kyanite–sillimanite transitions, as well as the melting point of diopside. Temperature was measured with a $Pt_{90}Rh_{10}$–Pt thermocouple. Experiments were performed using the "hot-piston in" technique. In this method, the pressure is increased to approximately 10% below the final run pressure, then the temperature is increased to the desired run temperature, and finally, the pressure is increased to the final value. Samples were quenched isobarically by turning off the power whilst maintaining a pressure within 0.02 GPa of the run pressure. Quench rates were of the order of 75° per second. The lithium content of the samples, the mean oxidation state of nickel and the total nickel content were determined by atomic absorption analysis, iodometric titration and complexometric titration, respectively.

X-ray phase analysis was performed using a Philips X′ Pert powder diffractometer with monochromatic $CoK_{\alpha 1}$ radiation, and Si being the internal standard. The scan range was $15 \leqslant 2\theta \leqslant 120$ with a step increment of 0.02°. A Fullprof computer program was used for the calculations [17]. The diffractometer point zero, the Lorentzian/Gaussian fraction of the pseudo-Voigt peak function, scale factor, the unit cell parameters (a and c), the oxygen parameter (z), the thermal factor for the 3a, 3b and 6c positions, the line half-width parameters and the preferred orientation were determined. The cationic occupancy factors were refined taking into account that the total occupancies of the 3a, 3b and 6c sites are equal to unity.

SEM analyses on powder samples coated with gold were carried out on a JEOL-100 B microscope with 10 kV accelerating voltage.

The IR spectra were recorded with a Nicolet Avatar-32 spectrometer using KBr pellets. Magnetic susceptibility was determined by the Faraday method at 100–300 K.

EPR measurements at 9.23 GHz (X-band) were carried out using a ERS 220/Q spectrometer over the temperature range 85–410 K. The g-factors were established with respect to a Mn^{2+}/ZnS standard. The signal intensity was determined by double integration of the experimental EPR spectrum. The high-frequency EPR spectra were recorded on a single-pass transmission EPR spectrometer built in the High-Magnetic Field Laboratory, Grenoble, France. The frequencies were changed from 95 to 475 GHz using Gunn diodes and their multipliers. The detection of absorption was performed with a bolometer. The recording temperatures were varied from 5 to 300 K using a variable temperature insert (Oxford Instruments).

3. Results and discussion

3.1. Structural characterization of $Li[Li_xNi_{1-x}]O_2$

Varying the Li/Ni ratio in the initial mixture of NiO and Li_2O_2 from 1.0 to 2.05 at high pressure resulted in

the formation of new $Li[Li_xNi_{1-x}]O_2$ compositions with $0 \leqslant x \leqslant \frac{1}{3}$. Thermal decomposition of Li_2O_2 under the experimental conditions used (700 °C and 3 GPa) ensured an oxygen-rich atmosphere which was necessary for the stabilization of the nickel ions at high oxidation states

$$(1-x)\ NiO + 1/2(1+x)\ Li_2O_2 + sLi_2O_2 \rightarrow Li[Li_xNi_{1-x}]O_2 + s\ Li_2O + s/2\ O_2.$$

To compensate for the lithium volatility at the relatively high synthesis temperature, a small excess of Li_2O_2, *s*, was used. As in the case of synthesis under atmospheric pressure, the Li/Ni ratio in the oxides obtained under high pressure was a little below that of the initial mixture (Table 1). The Li content in the oxides obtained was determined both by chemical analysis and Rietveld analysis of the XRD patterns. In accordance with the literature data on $LiNiO_2$ [7,18], the Rietveld analysis gives systematically higher value for the Li-to-Ni ratio. However, there is a similar trend in the changes of the Li/Ni ratio (Table 1). In addition, in contrast to solid state synthesis under atmospheric pressure, at high pressure, oxides with a Li/Ni > 1 can be obtained. For oxides prepared at atmospheric pressure and 700 °C, the Li-to-Ni ratio is always lower than 1, irrespective of the ratio used in the precursor mixture. For example, Arai et al. [4] reported the preparation of nearly stoichiometric $LiNiO_2$ with L/Ni ≈ 1 by using 3 moles of Li excess.

Fig. 1 shows XRD patterns of oxides obtained under high pressure, with varying initial Li/Ni ratios from 1.05 to 2.05. For all the samples obtained, the main diffraction reflections match well with the layered-type crystal structure (*R*-3 *m*). However, the compositions can be divided in three groups with respect to the initial Li-to-Ni ratio: $1.05 \leqslant Li/Ni \leqslant 1.20$, $1.2 < x < 2.05$ and $x = 2.05$. Chemical analysis and X-ray diffraction studies show that with $1.05 \leqslant Li/Ni \leqslant 1.20$ layered non-stoichiometric oxides, $(Li_{1-\delta}Ni_\delta)NiO_2$ with $\delta < 0.05$, are obtained (Table 1). The diffraction lines of all samples are best described by a hexagonal symmetry, space group (*R*-3 *m*). The structural model used comprises Li in 3*b* sites (000.5), Ni in 3*a* sites (000) and oxygen in 6*c* sites (00*z*). The amount of Ni in the LiO_2 layer (δ) depends on the initial Li/Ni ratio, the best stoichiometry corresponding to Li/Ni = 1.1. Moreover, samples of $[Li_{1-\delta}Ni_\delta]NiO_2$ obtained at high- and atmospheric pressure do not differ in their parameters and cationic arrangement.

For samples with initial Li/Ni > 1.25, low-intensity diffuse peaks in the range $22 < 2\Theta < 28°$ appear in addition to the main diffraction lines. For the end composition with initial Li/Ni = 2.05, the structural refinement has been carried out with a monoclinic layered *C*2/*c* space group according to Migeon et al. [8]. However, the fitting procedure is unsatisfactory

Table 1
Li-to-Ni ratio (determined from chemical, CA, and Rietveld analysis, RA) and structural parameters determined from XRD Rietveld refinement for $[Li_{1-\delta}Ni_\delta]_{3b}[Ni]_{3a}[O_2]_{6c}$ and $[Li_{1-\delta}Ni_\delta]_{3b}[Li_xNi_{1-x}]_{3a}[O_2]_{6c}$ compositions obtained at high-pressure from precursors with Li-to-Ni ratios between 1.05 and 2.05

Initial Li/Ni-ratio	CA Li/Ni-ratio (±0.01)	*a*/Å (±0.0001)	*c*/Å (±0.0008)	*z* (oxygen parameter)	δ (±0.003)	X (±0.005)	RA Li/Ni-ratio	Li–O/(Å)	M–O/(Å)	μ/BM (calc.)	μ/BM (exper.)
1.05	0.84	2.8775	14.1937	0.2585 (2)	0.055	0	0.896	1.972	2.112	1.87	1.79
1.10	0.96	2.8769	14.1827	0.2592 (5)	0.014	0	0.972	1.966	2.117	1.77	1.88
1.20	0.97	2.8755	14.1806	0.2585 (5)	0.022	0	0.957	1.970	2.110	1.79	1.90
1.25	1.09	2.8654	14.1793	0.2595 (5)	0.009	0.080	1.153	1.958	2.114	1.60	1.80
1.50	1.27	2.8319	14.0990	0.2587 (5)	0.043	0.185	1.331	1.944	2.087	1.45	1.16
2.05[a]	1.66	2.8226	14.0910	0.2580 (4)	0.028	0.337	1.894	1.939	2.084	0.64	0.79

The experimental average magnetic moments per one nickel ion (μ_{exp}) and the calculated one for a cation distribution $Li_{1-\delta}Ni_\delta[Li_xNi_{1-3x+\delta}Ni_{2x-\delta}]O_2$ ($\mu_{calc.}$) are also presented.
[a]For the sake of comparison, $Li[Li_xNi_{1-x}]O_2$ prepared from precursor with Li/Ni = 2.05 is indexed also in *R*-3/*m*.

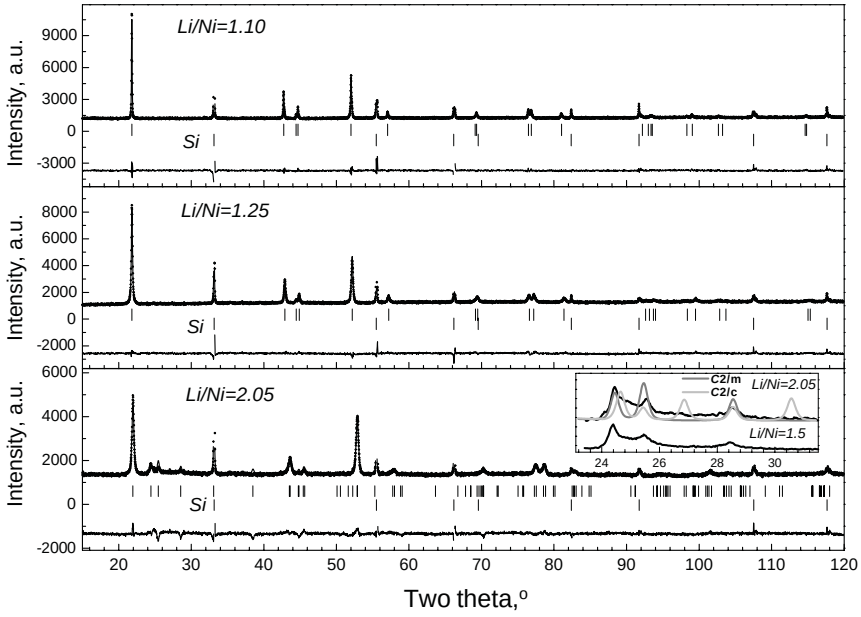

Fig. 1. XRD patterns of lithium-nickel oxides prepared at 3 GPa from precursors with Li-to-Ni from 1.05 to 2.05. The difference between the observed and calculated profiles is plotted. Bragg reflections for layered trigonal and monoclinic structures and Si standard are indicated. For comparison, the inset gives the range where the low-intensity peaks due to the monoclinic $C2/c$ and $C2/m$ appear.

Table 2
Position and structural parameters determined from XRD Rietveld refinement for $Li[Li_xNi_{1-x}]O_2$ prepared from precursor with Li/Ni = 2.05

Atom	Site	x	y	z	B_{iso} (Å^2)	Occupancy
Li1	2*b*	0.0000	0.5000	0.0000	0.29	0.25
Li2	2*c*	0.0000	0.0000	0.5000	1.01	0.25
Li3	4*h*	0.0000	0.6868(5)	0.5000	1.14	0.50
Ni	4*g*	0.0000	0.1704(3)	0.0000	1.09	0.50
O1	4*i*	0.2397(9)	0.0000	0.2125(8)	0.32	0.50
O2	8*j*	0.2489(5)	0.3321(9)	0.2288(5)	0.47	1.00

Cell parameters: $a = 4.8984$ (8) Å, $b = 8.4496$ (13) Å, $c = 4.9692$ (5) Å, $\beta = 109.02°$ (2); $V = 194.60$ (5) Å^3.

($R_B = 28.3$): the main diffraction lines are fitted well, while many additional reflections with appreciable intensity have been calculated at $22 < 2\Theta < 28°$ (Fig. 1). In order to fit the low-intensity diffraction peaks between $22 < 2\Theta < 28°$, a monoclinic system with a $C2/m$ space group has also been checked ($R_B = 17.6$). The refined cell parameters are given in Table 2. The refined structure of Li_2NiO_3 with a $C2/m$ space group agrees well with the single crystal structure determination for Li_2MnO_3, where a monoclinic cell with a $C2/m$ space group was used [19]. The monoclinic system with a $C2/c$ or $C2/m$ space group reflects a different arrangement in the Li-layers, but the arrangement in the mixed (LiM_2)-layers is the same, where every Li ion is surrounded by 6 Ni ions, and every Ni ion has 3 Li and 3 Ni ions as nearest neighbors. It appears that high pressure (3 GPa) favors the formation of monoclinic oxides with $C2/m$ space group, while oxides with $C2/c$ are obtained at lower pressure (150 bar). The influence of the experimental conditions on the space group symmetry of oxides has been established already for Li_2MnO_3 [19–21].

Intermediate compositions (obtained from precursors with $1.25 < Li/Ni < 2.05$) also display additional low-intensity peaks over the range of $22 < 2\Theta < 28°$. For that reason, the layered monoclinic ($C2/m$) and the trigonal space group (R-3m) are used for structural characterization. A better fit is obtained using the R-3m space group: $R_B = 19.3$ and 4.9, respectively. In order to achieve the best possible characterization of the peaks at $22 < 2\Theta < 28°$, a two-phase model comprising a main phase with a layered structure and an impurity phase with a monoclinic structure has also been investigated. In this case again there is no good fitting. Moreover, the positions of these peaks are changed with increasing the Li-to-Ni ratio, thus indicating the formation of solid solutions. This means that the diffraction lines in the 2Θ region $22 < 2\Theta < 28$ corresponds to super-lattice reflections rather than these peaks are due to the presence of an impurity phase. Super-lattice reflections have been detected for the complex "$LiNiO_2$–Li_2MnO_3" system (or notation as a solid solution $Li[Li_{1/3-2/3x}Ni_xMn_{2/3-x/3}]O_2$) [14]. The X-ray patterns have been interpreted by the formation of "$LiNiO_2$–Li_2MnO_3" solid solutions, where long-range Li ordering on the $3^{1/2}$ $a \times 3^{1/2}$ a super-structure appears together with an

uniformly mixing of Ni and Mn on the transition-metal sites [14]. On the other hand, from NMR and TEM analysis, formation of local Li_2MnO_3–rich regions has been suggested [16].

Table 1 shows that the appearance of Li^+ ions (x) in the NiO_2-layers starts at an initial $Li/Ni \geqslant 1.25$. The incorporation of Li in the lattice is accompanied by a change in the structural parameters as compared to the well-known $LiNiO_2$. The unit cell parameters a and c decrease while the trigonal distortion (expressed by c/a) increases. Irrespective of the manner of the Li-to-Ni ratio determination, the observed changes in the unit cell parameters do not obey the Vegard's law, which can be related with non-random Li–Ni distribution. By increasing the Li/(Li + Ni) ratio, there is a volume contraction

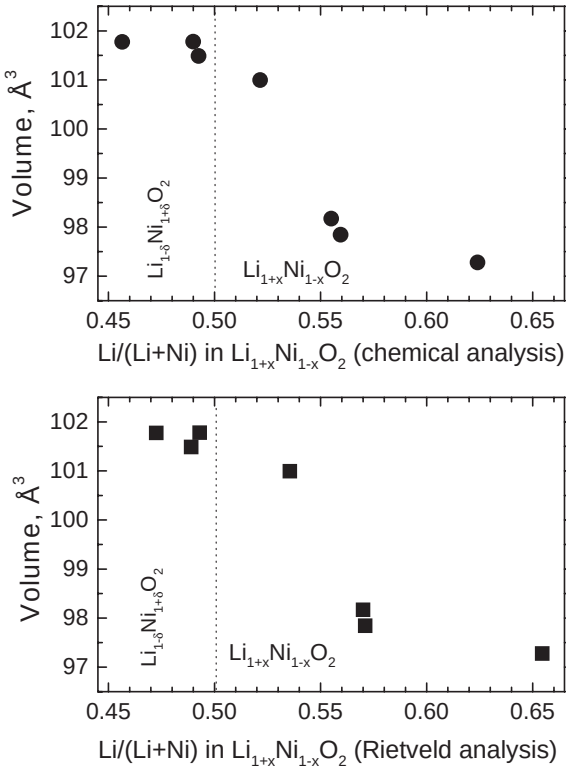

Fig. 2. Unit cell volume vs. Li-to-Ni ratio in $Li_{1+x}Ni_{1-x}O_2$ determined from chemical and Rietveld analysis. For the sake of comparison, $Li_{1+x}Ni_{1-x}O_2$ prepared from precursor with Li/Ni = 2.05 is indexed also in R-3/m.

(Fig. 2). The mean Li_xNi_{1-x}–O bond length decreases, which is associated with partial oxidation of Ni^{3+} to Ni^{4+} (Table 1). For the sake of comparison we shall mention that the lengths of the Ni^{3+}–O and Ni^{4+}–O bonds in lithium-transition metal oxides are 1.97 and 1.90 A, respectively [22]. The length of the $Li_{1-\delta}Ni_\delta$–O bond in the LiO_2- layer also decreases with the change in length of the Li_xNi_{1-x}–O bond in the mixed $[Li_xNi_{1-x}]O_2$ layers.

The morphology of the samples prepared under high pressure is shown in Fig. 3. As one can see, there is no difference in the morphology of samples prepared at low and high Li-to-Ni ratios. The samples consist of plate-like particles with an average diameter of 100–200 nm. The plate-like particles are stacked into aggregates with diameters larger than 1 μm.

The Li/Ni distribution in $[Li_xNi_{1-x}]O_2$ layers can be monitored by infrared spectroscopy. Fig. 4 presents comparison of IR spectra of oxides with $1.05 \leqslant Li/Ni \leqslant 2.05$ in the 400–800 cm^{-1} region where vibrations of the transition metal layers are established.

The almost stoichiometric $Li_{1-\delta}Ni_{1+\delta}O_2$ sample ($\delta < 0.02$) exhibits two intense peaks at 500 and 565 cm^{-1} due to NiO_2-vibrations. The IR spectrum of the end composition with $Li/Ni = 2$ shows 5 components at 425, 505, 562, 615 and 648 cm^{-1}, respectively (Fig. 4). The increase in number of the IR bands for $Li[Li_{1/3}Ni_{2/3}]O_2$ is consistent with a $[Li_{1/3}Ni_{2/3}]$-arrangement in the mixed $[Li_{1/3}Ni_{2/3}]O_2$ layers as was observed from XRD analysis. Samples with intermediate compositions ($0 < x < \frac{1}{3}$) display splitting of the two main IR bands, their number increasing with the Li amount in the layer. This result provides evidence for additional short range ordering of lithium and nickel at these compositions. The similar IR profiles suggest that short-range Li/Ni ordering in intermediate compositions mimic the cationic distribution of the end compositions.

Summarizing the XRD and IR data, layered $Li[Li_xNi_{1-x}]O_2$ oxides, over the whole concentration range, can be prepared by solid state reaction between Li_2O_2 and NiO under high-pressure conditions in oxygen-rich atmospheres. The incorporation of Li into NiO_2-layers causes contraction of the unit cell parameters, with

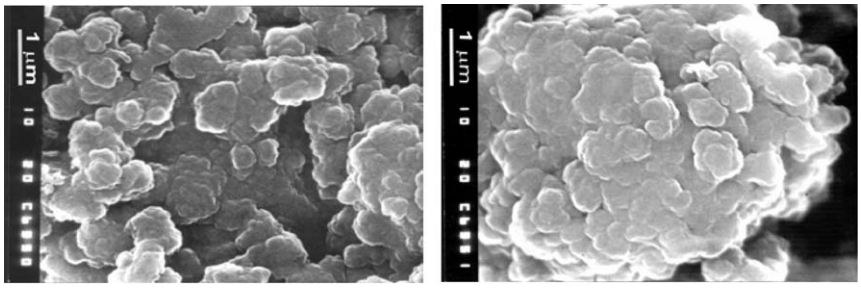

Fig. 3. SEM images of $Li_{1+x}Ni_{1-x}O_2$ prepared from precursors with Li/Ni = 1.2 (left) and 1.5 (right).

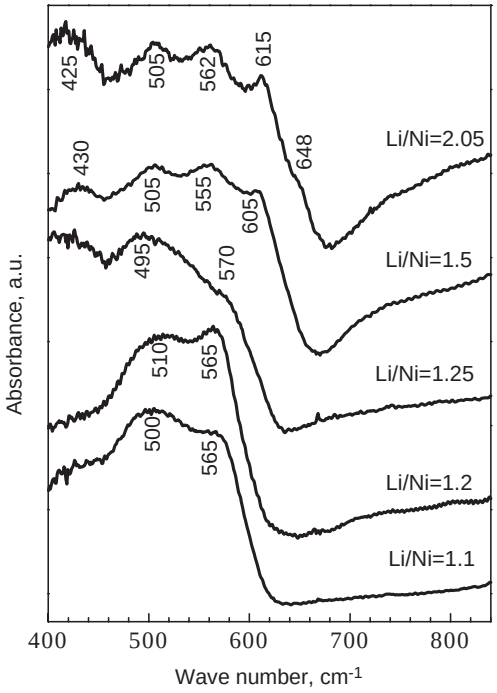

Fig. 4. IR spectra of $Li_{1+x}Ni_{1-x}O_2$ prepared at 3 GPa from precursors with Li/Ni ratios between 1.1 and 2.05.

Vagard's law not being obeyed. There is a strong tendency for Li and Ni to order in the NiO_2-layers.

3.2. Oxidation state of Ni in $Li[Li_xNi_{1-x}]O_2$

The oxidation state of Ni ions in the $Li[Li_xNi_{1-x}]O_2$ oxides has been studied by EPR. Nearly stoichiometric $LiNiO_2$ has an EPR spectrum consisting of a single line with Lorentzian shape and $g = 2.137$ due to exchange-coupled Ni^{3+} ions [23]. A signal with the same shape and g value, but with a larger line width, corresponds to $Li[Li_xNi_{1-x}]O_2$ (Fig. 5). The EPR line width increases with the number of lithium ions incorporated in the nickel layer (Fig. 6). The intensity of the EPR signal decreases in the same sequence. With the $Li[Li_{1/3}Ni_{2/3}]O_2$ end composition the broad signal disappears and a narrow low-intensity signal with $g = 2.14$ appears instead. According to the EPR study of Ni^{3+} in $LiNi_xCo_{1-x}O_2$ solid solutions [24], these parameters suggest that the broad EPR signal observed may be attributed to exchange-coupled Ni^{3+} ions, while the narrow low-intensity signal comes from magnetically isolated Ni^{3+} ions. To rationalize the dependence of the EPR line width and EPR intensity on the Li-content, Fig. 6 also gives changes in the number of Ni^{3+} ions. As expected, changes in EPR line width and EPR intensity correlate with the amount of Ni^{3+}. The increase in line width with the amount of lithium in the $Li_xNi_{1-x}O_2$ layers can be explained to be the results of magnetic dilution of paramagnetic Ni^{3+} ions by diamagnetic Ni^{4+}

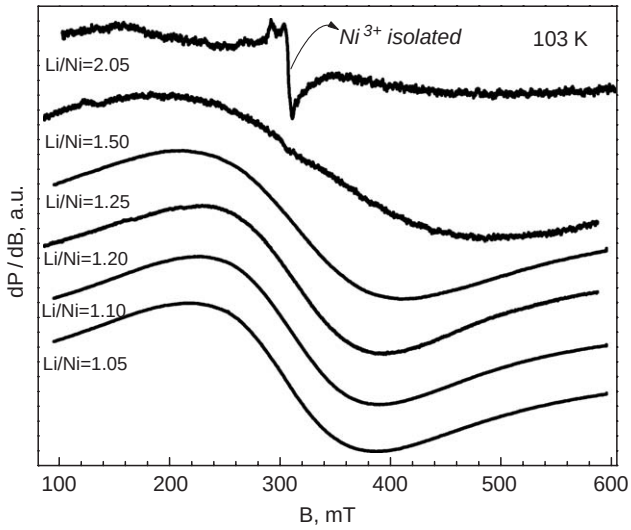

Fig. 5. EPR spectra in X-band of $Li_{1+x}Ni_{1-x}O_2$ prepared at 3 GPa from precursors with Li/Ni ratio varied between 1.05 and 2.05.

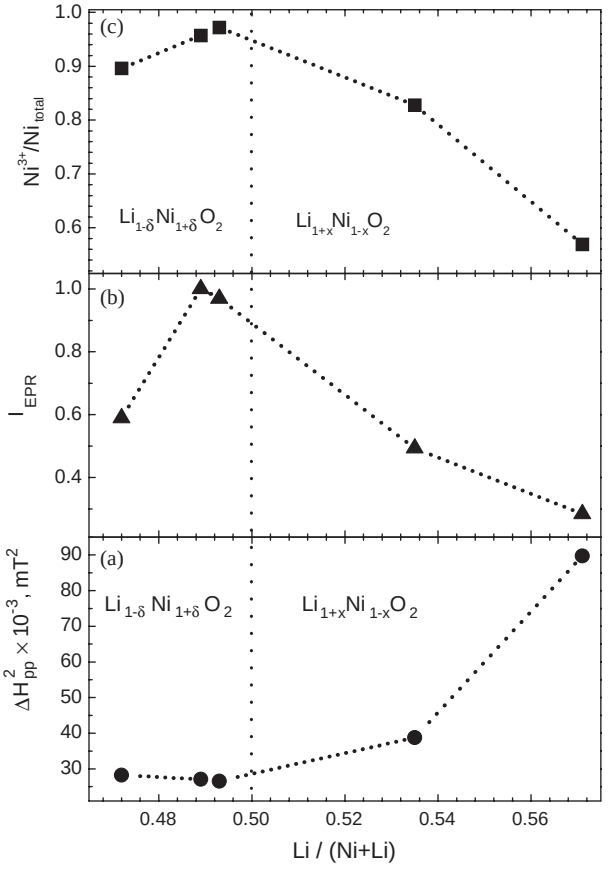

Fig. 6. EPR line width (a) and EPR relative intensity (b) determined at 103 K in X-band versus Li-content, Li/(Li + Ni), in $Li_{1+x}Ni_{1-x}O_2$. The Ni^{3+}/Ni_{total} amount (c) determined according to following cation distribution $Li_{1-\delta}Ni^{2+}_{\delta}[Li_xNi^{3+}_{1-3x+\delta}Ni^{4+}_{2x-\delta}]O_2$ as a function of the Li-content.

ions. On the other hand, this indicates the formation of solid solutions between $LiNiO_2$ and $Li[Li_{1/3}Ni_{2/3}]O_2$. For the end $Li[Li_{1/3}Ni_{2/3}]O_2$ composition there is an EPR

signal of isolated Ni^{3+} ions only, whose surroundings include diamagnetic ions (Li^{+} and/or Ni^{+4} ions).

One can differentiate between the two kinds of compositions, $Li_{1-\delta}Ni_{\delta}[Li_xNi_{1-x}]O_2$ and $Li_{1-\delta}Ni_{1+\delta}O_2$, on the basis of the EPR line width and its temperature dependence (Fig. 7). With $Li_{1-\delta}Ni_{1+\delta}O_2$ oxide, the signal shows a linear decrease of the line width with decreasing registration temperature within the range 400–100 K. The slope of the linear dependence, $d\Delta H_{pp}/dT$, increases with the amount of Ni^{2+} in the lithium layers: from 0.492 to 0.421 mT/K for samples prepared from Li/Ni = 1.05 and 1.10, respectively. This result is in agreement with previous EPR investigations on $Li_{1-\delta}Ni_{1+\delta}O_2$ oxides [6] where it has been shown that the $d\Delta H_{pp}/dT$ slope depends on the strength of the 180° and 90° Ni–O–Ni exchange interaction, the coordination number of exchange coupled particles and the distance between them. An unexpected result is obtained for the sample prepared from precursor with Li/Ni = 1.2, where there is a marked deviation from the linear dependence of the EPR line width. This indicates peculiarities in the cationic distribution, which can be associated with the presence of impurity lithium ions in the nickel layer. For this sample, the number of lithium ions in the nickel layer is low enough to prevent them from being detected by analysis of the X-ray diffraction lines. This result may explain the sharp change in composition of the oxides obtained from precursors with a Li/Ni ratio of 1.2 and 1.25: while the X-ray structure analysis shows the formation of $Li_{1-\delta}Ni_{1+\delta}O_2$ oxides from precursors with Li/Ni = 1.2, EPR of Ni^{3+} ions provides evidence for the presence of small amounts of Li in the nickel layers. It should be noted that on the basis of temperature dependence analysis of the EPR signal, one cannot determine whether the lithium ion impurities are distributed regularly or is segregated in the mixed $Li_xNi_{1-x}O_2$-layer.

Additional differentiation between the samples containing lithium in the nickel layers can be achieved by EPR spectroscopy at high frequencies (HF-EPR). HF-EPR has been shown to provide better resolution as compared to conventional X-band EPR [25]. The advantage of using high-frequency EPR has been demonstrated for $Li_{1-\delta}Ni_{1+\delta}O_2$ with $0.02 \leqslant \delta \leqslant 0.12$: while in the X-band the symmetric EPR line gives rise to the EPR profile, the high-frequency measurements reveals an asymmetry of the signal [26]. Figs. 8 and 9 show the EPR spectra at 115 GHz of nearly stoichiometric $Li_{1-\delta}Ni_{1+\delta}O_2$ and $Li_{1-\delta}Ni_{\delta}[Li_xNi_{1-x}]O_2$ samples obtained from precursors with Li:Ni ratios of 1.2 and 1.5, respectively. Above 30 K the EPR spectrum of paramagnetic $Li_{1-\delta}Ni_{1+\delta}O_2$ consists of an asymmetric line (Fig. 8). Below 30 K the appearance of resonance absorption in high- and low field indicates the presence of magnetically correlated spins (Fig. 8). However, long-range magnetic ordering is not achieved with this sample. In contrast to nearly stoichiometric $Li_{1-\delta}Ni_{1+\delta}O_2$, the sample $Li_{1-\delta}Ni_{\delta}[Li_xNi_{1-x}]O_2$ containing Li in the nickel layers displays only one broad symmetric Lorentzian line above 13 K even in the high-frequency region (Fig. 9). The line width decreases with increasing temperature from 13 to 80 K, the g-value remaining constant: 2.155 (Fig. 10). In this temperature range the signal intensity varies with the registration temperature following the Curie–Weiss law with a Weiss constant $\Theta_{EPR} = +4$ K. The constant thus determined is lower than the Weiss constant determined for $Li_{1-\delta}Ni_{1+\delta}O_2$ prepared from precursor with Li/Ni = 1.2: $\Theta_{EPR} = +43$ K, X-band. At temperatures below 13 K the EPR line shape for $Li_{1-\delta}Ni_{\delta}[Li_xNi_{1-x}]O_2$ undergoes a change, most possibly due to short-range magnetic correlations. Similarly to the case of $Li_{1-\delta}Ni_{1+\delta}O_2$, a long-range magnetic ordering down to 5 K cannot be achieved with the $Li_{1-\delta}Ni_{\delta}[Li_xNi_{1-x}]O_2$ sample. This result shows

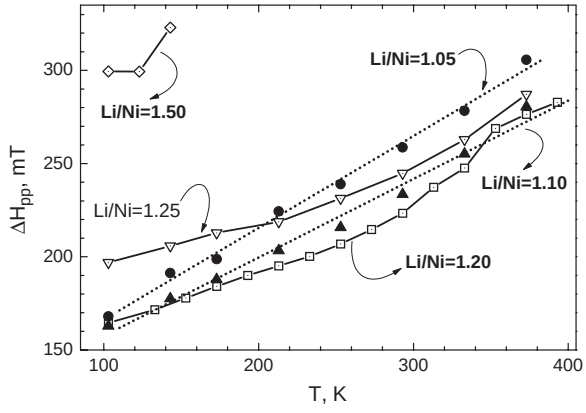

Fig. 7. Temperature variation of the EPR line width of $Li[Li_xNi_{1-x}]O_2$ prepared at 3 GPa from precursors with Li/Ni ratios between 1.05 and 1.50.

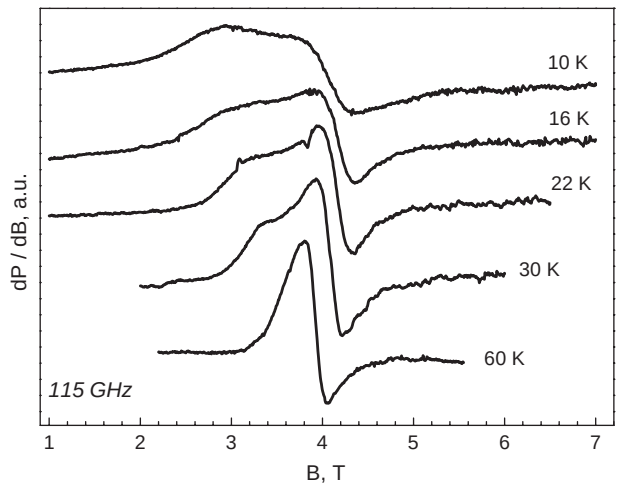

Fig. 8. EPR spectra at 115 GHz for nearly stoichiometric $Li_{1-\delta}Ni_{1+\delta}O_2$ prepared at 3 GPa from precursor with Li/Ni = 1.20.

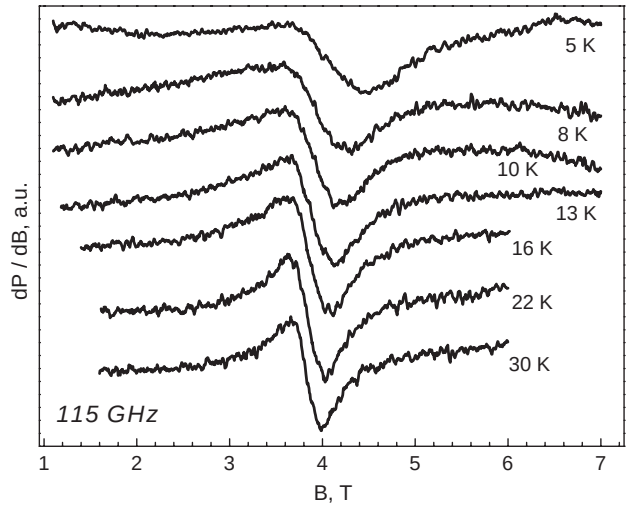

Fig. 9. EPR spectra at 115 GHz for $Li[Li_xNi_{1-x}]O_2$ prepared at 3 GPa from precursor with Li/Ni = 1.50.

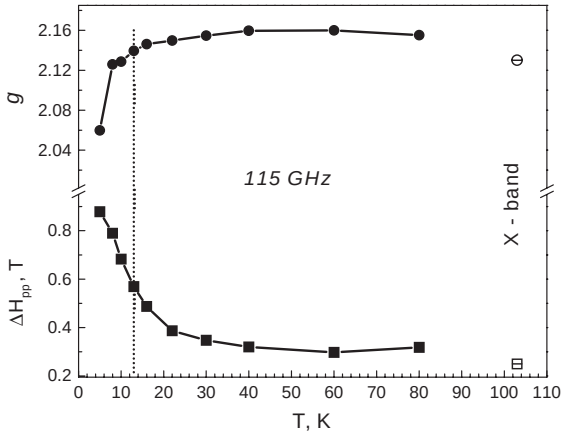

Fig. 10. Temperature variation of the EPR line width and of the g-value (determined at 115 GHz) for $Li[Li_xNi_{1-x}]O_2$ prepared at 3 GPa from precursor with Li/Ni = 1.50. For the sake of comparison, ΔH_{pp} and g determined at X-band are given also.

clearly that the EPR spectrum of $Li_{1-\delta}Ni_\delta[Li_xNi_{1-x}]O_2$ is due to low-spin Ni^{3+} ions. However, in contrast to nearly stoichiometric $Li_{1-\delta}Ni_{1+\delta}O_2$, the low-spin Ni^{3+} ions in $Li_{1-\delta}Ni_\delta[Li_xNi_{1-x}]O_2$ are magnetically diluted. The lack of any additional EPR signals in high-frequency EPR spectrum further supports that $Li_{1-\delta}Ni_\delta[Li_xNi_{1-x}]O_2$ represents a solid solution rather than complex intergrowth system with local inhomogeneous regions enriched in Ni^{3+} or Ni^{4+} ions.

The preparation of $Li[Li_xNi_{1-x}]O_2$ oxides under high oxygen pressure is also proved by magnetic susceptibility measurements. Using the spin-only values of the magnetic moments of the Ni^{2+} and Ni^{3+} ions (2.83 and 1.73 BM, respectively), Table 1 shows the values of the average magnetic moments of the nickel ions calculated for a cation distribution $Li_{1-\delta}Ni^{2+}_\delta[Li_xNi^{3+}_{1-3x+\delta}Ni^{4+}_{2\ x-\delta}]O_2$ (μ_{calc}) as well as the experimental values of the magnetic moments (μ_{exp}). The decrease in the magnetic moment of the nickel ions with the lithium amount in the nickel-rich layers reveals the appearance of diamagnetic Ni^{4+} ions ($\mu_{Ni(4+)} = 0$).

4. Conclusions

High-pressure synthesis in an oxygen rich atmosphere yields solid solutions between $LiNiO_2$ and Li_2NiO_3 over the whole concentration range. The crystal structure of $Li[Li_xNi_{1-x}]O_2$, $0 \leqslant x \leqslant \frac{1}{3}$, is changed from trigonal $R\text{-}3m$ to monoclinic $C2/m$ at Li-to-Ni ratio of 2 (or $x = \frac{1}{3}$). The incorporation of Li into NiO_2-layers causes a decrease in the mean Li–O and $Ni_{1-x}Li_x$–O bond distance. Li and Ni ions in the mixed $Ni_{1-x}Li_xO_2$-layers display a tendency to order at a small-scale range in such a way that mimics the $Li_{1/3}Ni_{2/3}$-arrangment in the end $Li[Li_{1/3}Ni_{2/3}]O_2$ composition.

At a first glance, the formation of solid solutions between trigonal $LiNiO_2$ and monoclinic Li_2NiO_3 bears a resemblance with the formation of complex "$LiNiO_2$–Li_2MnO_3" electrode materials [14]. However, the most important difference comes from the charge distribution in these oxides. Both Ni^{3+} and Ni^{4+} ions are stabilized in "$LiNiO_2$–Li_2NiO_3" solid solutions, while charge distribution in complex "$LiNiO_2$–Li_2MnO_3" proceeds via stabilization of Ni^{2+} and Mn^{4+} [15]. In addition, HF-EPR spectroscopy indicates that monoclinic Li_2NiO_3 is integrated in layered $LiNiO_2$ without the formation of domains enriched in Ni^{3+} or Ni^{4+} ions.

Acknowledgments

E.Zh., R.S. and E.Sh. acknowledge the National Science Fund of Bulgaria (Contract no. Ch1304/2003) for financial support. E.Sh. is grateful to the EC for a grant of a Marie Curie Host Fellowship Programme (Contract No. HPMT – CT – 2001 – 00231 to D.C. Rubie) in order to perform high-pressure synthesis experiments at the Bayrisches Geoinstitute. The high-frequency EPR measurements carried out at High Magnetic Field Laboratory in Grenoble, France, were supported by European Community "Access to Research Infrastructure action of the Improving Human Potential Programme". The authors are very grateful to Dr. T. Boffa-Ballaran, from Bayerisches Geoinstitut—Universität Bayreuth, and Dr. A.-L. Barra, from High Magnetic Field Laboratory in Grenoble, for their help.

References

[1] C. Delmas, M. Menetrier, L. Croguennec, I. Saadoune, A. Rougier, C. Poillerie, G. Prado, M. Grüne, L. Fournes, Electrochim. Acta 145 (1999) 243.

[2] R. Alcántara, P. Lavela, J.-L. Tirado, E. Zhecheva, R. Stoyanova, J. Solid State Electrochem. 3 (1999) 121.
[3] M.S. Whittingham, Chem. Rev. 104 (2004) 4271.
[4] H. Arai, S. Okada, H. Ohtsuka, M. Ichimura, J. Yamaki, Solid State Ionics 80 (1995) 261.
[5] A. Rougier, P. Gravereau, C. Delmas, J. Electrochem. Soc. 143 (1996) 1168.
[6] R. Alcántara, P. Lavela, J.L. Tirado, R. Stoyanova, E. Kuzmanova, E. Zhecheva, Chem. Mater. 9 (1997) 2145.
[7] V. Bianchi, D. Caurant, N. Baffier, C. Belhomme, E. Chappel, G. Chouteau, S. Bach, J.P. Pereira-Ramos, A. Sulpice, P. Wilmann, Solid State Ionics 140 (2001) 1.
[8] H.-N. Migeon, A. Courtois, M. Zanne, C. Gleitzer, Rev. Chim. Miner 13 (1976) 1.
[9] J.R. Dahn, U. von Sacken, C.A. Michal, Solid State Ionics 44 (1990) 87.
[10] R. Stoyanova, E. Zhecheva, R. Alcántara, J.L. Tirado, G. Bromiley, F. Bromiley, T. Boffa Ballaran, Solid State Ionics 161 (2003) 197.
[11] M.E. Spahr, P. Novak, B. Schneyder, O. Haas, R. Nesper, J. Electrochem. Soc. 145 (1998) 1113.
[12] Z. Lu, J.R. Dahn, J. Electrochem. Soc. 149 (2002) A815.
[13] L. Zhang, H. Nguchi, M. Yoshio, J. Power Sources 110 (2002) 57.
[14] Z. Lu, Z. Chen, J.R. Dahn, Chem. Mater. 15 (2003) 3214.
[15] W.-S. Yoon, C.P. Grey, M. Balasubramanian, X.-Q. Yang, J. McBreen, Chem. Mater. 15 (2003) 3161.
[16] J.-S. Kim, C.S. Johnson, J.T. Vaughey, M.M. Thackeray, S.A. Hackney, W. Yoon, C.P. Grey, Chem. Mater. 16 (2004) 1996.
[17] J. Rodríguez-Carvajal, in: Satellite Meeting on Powder Diffraction of the XV Congress of the IUCr, 1990, p. 127.
[18] A. Rougier, P. Gravereau, C. Delmas, J. Electrochem. Soc. 143 (1996) 1168.
[19] P. Strobel, B. Lambert-Andron, J. Solid State Chem. 75 (1988) 90.
[20] A. Riou, A. Lecerf, Y. Gerault, Y. Cudennec, Mater. Res. Bull. 27 (1992) 269.
[21] V. Massaroti, M. Bini, D. Capsoni, A. Altomare, G.G. Moliterni, J. Appl. Crystallogr. 30 (1997) 123.
[22] A.N. Mansour, X.Q. Yang, X. Sun, J. McBreen, L. Croguennec, C. Delmas, J. Electrochem. Soc. 147 (2000) 2104.
[23] R. Stoyanova, E. Zhecheva, C. Friebel, J. Phys. Chem. Solids 54 (1993) 9.
[24] R. Stoyanova, E. Zhecheva, R. Alcántara, P. Lavela, J.L. Tirado, Solid State Commun. 102 (1997) 457.
[25] K.K. Anderson, A.-L. Barra, Spectrochim. Acta A 58 (2002) 1101.
[26] A.-L. Barra, G. Chouteau, A. Stepanov, A. Rougier, C. Delmas, Eur. Phys. J. B 7 (1999) 551.